




Azimuthal temperature variations in ISO-Oph 2 from multifrequency ALMA observations

Simon Casassus ^{1,2,3}★, Lucas Cieza^{3,4}, Miguel Cárcamo^{2,3,5,6}, Álvaro Ribas⁷, Valentin Christiaens⁸, Abigali Rodríguez-Jiménez^{1,3}, Carla Arce-Tord ^{1,3}, Trisha Bhowmik^{3,4,5}, Prachi Chavan ^{3,4}, Camilo González-Ruilova^{3,4} and Rafael Martínez-Brunner^{1,3}

¹Departamento de Astronomía, Universidad de Chile, Casilla 36-D, Santiago, Chile

²Data Observatory Foundation, to Data Observatory Foundation, Eliodoro Yáñez 2990, Providencia, Santiago, Chile

³Millennium Nucleus on Young Exoplanets and Their Moons (YEMS), Santiago, Chile

⁴Núcleo de Astronomía, Facultad de Ingeniería y Ciencias, Universidad Diego Portales, Av Ejército 441, Santiago, Chile

⁵Computer Engineering Department, Faculty of Engineering, University of Santiago of Chile (USACH), Santiago, Chile

⁶Center for Interdisciplinary Research in Astrophysics and Space Exploration (CIRAS), Universidad de Santiago de Chile, Santiago, Chile

⁷Institute of Astronomy, University of Cambridge, Madingley Road, Cambridge CB3 0HA, UK

⁸Space Sciences, Technologies & Astrophysics Research (STAR) Institute, Université de Liège, Allée du Six Août 19c, B-4000 Sart Tilman, Belgium

Accepted 2023 June 22. Received 2023 June 21; in original form 2023 April 5

ABSTRACT

Environmental effects, such as stellar fly-bys and external irradiation, are thought to affect the evolution of protoplanetary discs in clustered star formation. Previous Atacama Large Millimetre/submillimetre Array (ALMA) images at 225 GHz of the ISO-Oph 2 binary revealed a peculiar morphology in the disc of the primary, perhaps due to a possible fly-by with the secondary. Here, we report on new ALMA continuum observations of this system at 97.5, 145, and 405 GHz, which reveal strong morphological variations. Multifrequency positional alignment allows us to interpret these spectral variations in terms of underlying physical conditions. ISO-Oph 2A is remarkably offset from the centroid of its ring, at all frequencies, and the disc is lopsided, pointing at gravitational interactions. However, the dust temperature also varies in azimuth, with two peaks whose direction connects with HD 147889, the earliest-type star in the Ophiuchus complex, suggesting that it is the dominant heat source. The stellar environment of ISO-Oph 2 appears to drive both its density structure and its thermal balance.

Key words: techniques: interferometric – protoplanetary discs – stars: individual: PDS 70, ISO-Oph 2 – stars: pre-main-sequence.

1 INTRODUCTION

Interferometric observations at (sub)millimetre wavelengths can resolve circumstellar discs at subarcsecond resolution and trace the thermal continuum emission due to dust (e.g. Andrews et al. 2009, 2010; Isella, Carpenter & Sargent 2009). Also, multiwavelength (sub)millimetre data can help constrain dust properties such as the maximum grain size (Guilloteau et al. 2011). With unprecedented capabilities, the Atacama Large Millimetre/submillimetre Array (ALMA) has revolutionized the field over the last decade. ALMA has already surveyed most star-forming regions in nearby (distances $d < 300$ pc) molecular clouds, including Chameleon (Pascucci et al. 2016; Villenave et al. 2021), Lupus (Ansdell et al. 2016, 2018), Taurus (Long et al. 2018, 2019), and Ophiuchus (Cox et al. 2017; Cieza et al. 2019). Even though these surveys have mostly been carried out in a single frequency at a modest resolution (0.1–0.2 arcsec), they still allow us to investigate disc properties as a function of different variables, such as IR Class (Williams et al. 2019), stellar mass (Barenfeld et al. 2016; Pascucci et al. 2016), age (Ansdell et al.

2018; Ruíz-Rodríguez et al. 2018), and stellar multiplicity (Cox et al. 2017; Zurlo et al. 2020, 2021).

In models of clustered star formation, the stellar environment affects disc structure and evolution (e.g. Haworth 2021; Winter & Haworth 2022; Wilhelm et al. 2023), both through external irradiation, which may lead to photoevaporation, and through gravitational interaction, including disc truncation and accretion bursts. The Orion proplyds (O’deh & Wen 1994) are spectacular examples of the impact of environment through external photoevaporation. Demographic surveys in the Orion nebula cluster show that disc structure is determined in part by the distance to θ^1 Ori C (Mann et al. 2014; Eisner et al. 2018). In turn, models of fly-bys may explain the structures seen in several binary discs (e.g. Dong et al. 2022; Cuello, Ménard & Price 2023). However, the probability for witnessing such close encounters (with a crossing time of $\lesssim 400$ yr within 500 au at a typical relative velocity of ~ 6 km s⁻¹) is very small compared to the disc lifetime (~ 10 Myr), and isolated spiral systems have been shown not to have undergone recent stellar encounters (in the past 10^4 yr; Shuai et al. 2022). In any case, whichever the mechanism, the environment plays a significant role in exoplanet demographics (Winter et al. 2020; Longmore, Chevance & Kruijssen 2021).

* E-mail: simon@das.uchile.cl

Table 1. Observation log. All data sets are original except for 225 GHz, i.e. all scheduling blocks for B6, which have previously been reported in Cieza et al. (2021) and González-Ruilova et al. (2020) (but with different synthesis imaging tools).

ν^a	Date	Δt^b	Baseline range (m)	Pwv ^c	Data set code	Beam and noise ^d		
						$r = 0$	$r = 1$	$r = 2$
405	04-Aug-2022	56.4 s	15–1300	0.6	B8	$0.157 \times 0.132/88$ and 340	$0.195 \times 0.164/84$ and 260	$0.209 \times 0.173/83$ and 270
	11-Aug-2022	56.4 s	15–1300	0.5				
225	12-Jun-2019	15 min	83–16 196	1.2	LB19	$0.028 \times 0.017/-32$ and 20	$0.034 \times 0.025/-23$ and 11	$0.036 \times 0.027/-19$ and 10
	21-Jun-2019	24 min	83–16 196	0.9	B6			
	13-Jul-2017	20 s	16–2647	1.95	SB17			
	13-Jul-2017	20 s	16–2647	1.8				
145	14-Jul-2017	20 s	16–2647	1.1		$0.228 \times 0.161/77$ and 100	$0.346 \times 0.237/79$ and 67	$0.385 \times 0.266/79$ and 67
	20-Jul-2022	24 s	15–2617	3.0	B4			
	21-Jul-2022	24 s	15–2617	2.4				
97.5	21-Jul-2022	24 s	15–2617	2.7		$0.157 \times 0.108/88$ and 38	$0.260 \times 0.199/-86$ and 24	$0.288 \times 0.224 /-83$ and 23
	27-Jul-2021	128 s	15–3321	0.6	B3			
	31-Oct-2021	128 s	63–6855	1.0				
	03-Nov-2021	128 s	47–5185	1.4				

^aCentre frequency in GHz. ^bTime on-source. ^cColumn of precipitable water vapour, in mm. ^dThe beam major axis (bmaj, arcsec), minor axis (bmin, arcsec), and direction (bpa, degrees), and noise (rms, $\mu\text{Jy beam}^{-1}$) are reported in the format $\text{bmaj} \times \text{bmin}/\text{bpa}$ and rms, for a choice of 3 Briggs robustness parameter r .

The demographic surveys also allow us to identify particularly interesting targets for follow-up studies. Such is the case for the ISO-Oph 2 system, a wide-separation (240 au) binary targeted by the Ophiuchus Disc Survey Employing ALMA (ODISEA; Cieza et al. 2019) in band 6 (230 GHz). ISO-Oph 2 was observed at 0.02 arcsec resolution, also in band 6, as part of the high-resolution follow-up of the brightest ODISEA targets (Cieza et al. 2021). The high-resolution observation showed that the disc around the primary consists of two non-axisymmetric rings and that the disc around the secondary is a narrow ring with a 2 au inner radius and a 1 au width (González-Ruilova et al. 2020). Furthermore, the ^{12}CO data show a bridge of gas connecting both discs, suggesting that the binary is interacting, and is perhaps in a fly-by orbit.

Another particularly interesting aspect of ISO-Oph 2 is that, among the long-baseline ODISEA sample (Cieza et al. 2021), it is the closest to HD 147889 (B2IV, B3IV; Casassus et al. 2008), the earliest-type star in the Ophiuchus complex. This proximity raises a question on the role of external irradiation in the thermal balance in the outer ring of ISO-Oph 2. ISO-Oph 2 is thus an interesting case study for the effect of the stellar environment on protoplanetary disc evolution, both in gravitational interactions and in external irradiation.

The ODISEA project has recently been extended to multifrequency observations covering over 90 objects in ALMA Band 4 (at 145 GHz; Chavan et al., in preparation) and Band 8 (405 GHz; Bhowmik et al., in preparation; Cieza et al., in preparation) in order to better constrain the physical properties of the Ophiuchus discs when combined with existing data. A crucial aspect of such an analysis is the alignment of the multifrequency data, which might not be acquired with the same phase centre, or could be affected by pointing errors, that could bias spectral trends such as spectral index maps. Casassus & Cárcamo (2022) proposed a strategy for the alignment of multi-epoch and multiconfiguration radio-interferometric data, although their application was restricted to the same correlator set-ups. It is interesting to investigate whether the same strategy might be applied to multifrequency data.

A crucial aspect of image synthesis is the process of image restoration, which conveys imaging residuals in the final images, along with a well-defined angular resolution. In the last couple of years, a technique, usually referred to as the ‘JvM correction’, has recently been incorporated in image restoration (Jorsater & van

Moorsel 1995; Czekala et al. 2021). The JvM correction reduces the noise and residuals in the final images. Here, we stress that the present analysis does not make use of this technique, as the resulting improvement in dynamic range is spurious. The proof, provided by Casassus & Cárcamo (2022), may not have been clear enough since applications of the JvM correction have become widespread. Here, we attempt to clarify some of the aspects of the proof in Appendix A.

This article reports on a multifrequency analysis of ISO-Oph 2. The new observations, along with our alignment strategy, are described in Section 2. The data show strong morphological variations with frequency, which we interpret in terms of underlying physical conditions in Section 3. We conclude, in Section 4, on a particularly strong impact of the environment in the case of ISO-Oph 2.

2 OBSERVATIONS

2.1 Data acquisition

The Band-6 ALMA observations of ISO-Oph 2 are described in Cieza et al. (2021) and González-Ruilova et al. (2020). The new ALMA observations, in Band 3, Band 4, and Band 8, were acquired as part of ALMA programmes 2019.1.01111.S, 2021.1.00378.S, and 2022.1.01734.S. An observation log can be found in Table 1, and includes a nomenclature for the data sets.

2.2 Imaging, self-calibration, and alignment

Automatic self-calibration was performed with the OOSELFCAL package, described in Casassus & Cárcamo (2022), which we re-baptized to ‘Self-calibratiON Object-oriented frameWork’, i.e. SNOW.¹ In brief, SNOW applies the self-calibration tasks `gaincal` and `applycal` from the CASA package, but replaces the imager `clean` by `UVMEM` (Casassus et al. 2006; Cárcamo et al. 2018). Here, `UVMEM` was run with pure- χ^2 optimization, i.e. without any regularization other than the requirement of image positivity. Image restoration was performed with natural weights (Briggs robustness

¹See Data availability section.

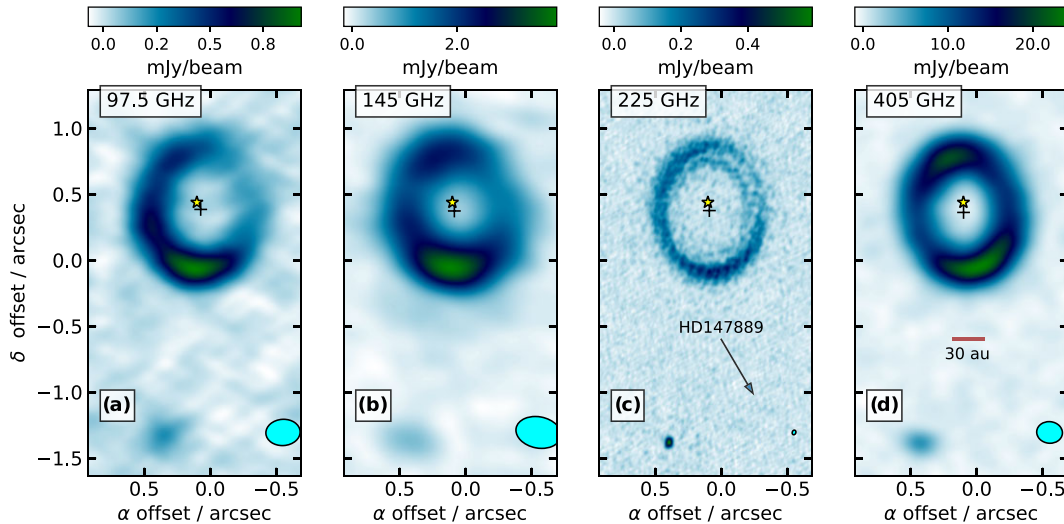


Figure 1. Summary of the multifrequency observations of ISO-Oph 2. The yellow star marks the position of ISO-Oph 2A, while the plus sign marks the position of the ring centroid (see Section 2.5). ISO-Oph 2B is the point source to the South. (a) B3 continuum, restored with $r = 1$. (b) B4 continuum, restored with $r = 1$. (c) B6 continuum, restored with $r = 2$. The arrow points to the direction of HD 147889. (d) B8 continuum, restored with $r = 1$. We provide a linear scale in au, assuming a distance of 134.3 ± 7.7 pc (Gaia Collaboration 2023).

parameter $r = 2$) for the self-calibration iterations, and with various choices of weights for the final images.

Each individual scheduling block, corresponding to the rows in Table 1, was self-calibrated individually before concatenation. Significant improvements were obtained only for B8, where the peak signal-to-noise ratio (PSNR) increased from 29 and 36 to 79 and 74 after four rounds of phase-only calibration (with solution intervals set to the scan length, 64, 32, and 15 s) and one round of amplitude and phase calibration (for the scan length). We aligned both scheduling blocks in B8 with the VISALIGN package (Casassus & Cárcamo 2022), but with the corrections described in Appendix C. Choosing 2022 August 4 as the reference, the corresponding astrometric shift is $\Delta x = -100 \pm 3$ mas in the direction of RA and $\Delta y = -31 \pm 3$ mas in Dec., while the flux scale correction factor is $\alpha_R = 1.20 \pm 0.01$. We note the very large astrometric shift, of about half a beam (in natural weights). Such a shift is larger than the nominal pointing accuracy of 1/10 the clean beam, and may reflect poor weather in either of the two epochs (the same procedure applied before self-calibration yields an even larger shift, $\alpha_R = 1.20 \pm 0.02$, $\Delta_x = -99 \pm 6$ mas, and $\Delta_y = -53 \pm 5$ mas). For B8, the concatenated scheduling blocks have PSNR of 100, with no further improvement for phase-only calibration, but a small increase to 102 after amplitude and phase self-calibration.

The resulting continuum data set was aligned to our choice of astrometric reference, which is the B6 data set. We applied VISALIGN without scaling in flux. B6 and B8 have very different phase centres, which may lead to the propagation of large numerical errors when performing the alignment in the uv -plane (as with VISALIGN). We therefore performed the alignment in two steps. First, we applied a coarse shift, corresponding to the difference between the nominal phase centres, or $\Delta x = -149.7$ mas and $\Delta y = -57$ mas. We then optimized the small shift, which yielded $\alpha_R = 0.240 \pm 0.003$, $\Delta_x = 179 \pm 2$ mas, and $\Delta_y = 50 \pm 2$ mas. We stress that, in this application of VISALIGN, across different ALMA bands, we set $\alpha_R = 1$.

For our astrometric reference data set, B6, the coarse shift in the alignment of SB17 to LB19 was $\Delta x = -16$ mas and $\Delta y = 82$ mas.

The optimization of the residual shift yielded $\alpha_R = 1.02 \pm 0.06$, $\Delta x = 13 \pm 9$ mas, and $\Delta y = -56 \pm 8$ mas. Self-calibration did not yield any improvement for B6, and the imaging residuals are thermal.

For B4, self-calibration yielded a small improvement in PSNR for all concatenated scheduling blocks, from 60 to 65 after amplitude and phase calibration. However, the alignment of each scheduling block, for which we chose 21-Jul as the reference, revealed an intriguing anomaly in flux. The shift of 20-Jul to 21-Jul was $\alpha_R = 1.00 \pm 0.02$, $\Delta x = -50 \pm 9$ mas, and $\Delta y = 63 \pm 8$ mas. However, the shift of the second 21-Jul block to the first, which were observed consecutively, yielded $\alpha_R = 1.05 \pm 0.02$, $\Delta x = -51 \pm 9$ mas, and $\Delta y = 22 \pm 6$ mas, corresponding to a 5 per cent flux scale difference. Although barely at 3σ , this flux scale difference is exactly as obtained when comparing the total flux densities. Such a flux scale difference is still well within the absolute flux calibration accuracy of ALMA, considered to be of ~ 5 per cent in Band-4 (e.g. Remijan et al. 2019).

The self-calibration procedure for B3 improved PSNR from 28 to 30 for 2021 July 27, after three rounds of phase-only self-calibration (with solution intervals set to the scan length, 64, 32, and 15 s), and very small improvements from 20 to 21 for 2021 October 31 and from 26 to 28 for 2021 November 3, both after a single round of phase-calibration. We chose 2021 July 27 as the reference, and shifted 2023 October 31 by $\alpha_R = 1.03 \pm 0.03$, $\Delta_x = -11 \pm 7$ mas, and $\Delta_y = 35 \pm 6$ mas, and 2021 November 3 by $\alpha_R = 0.98 \pm 0.02$, $\Delta_x = 38 \pm 7$ mas, and $\Delta_y = 15 \pm 7$ mas. The concatenated data set reaches a PSNR of 44 in natural weights, with no further improvements with self-calibration.

A summary of the self-calibrated and aligned data can be found in Fig. 1. The same figure but in brightness temperature is provided in Appendix B. A resolved multifrequency analysis requires all data sets to have a common angular resolution. In Fig. 2, we compare B3 with degraded version of B6 and B8, both smoothed to match B3. We also report in Fig. 3 the intensity spectral index maps, in the form $\alpha_{\nu_1}^{\nu_2} = \ln(I_{\nu_2}/I_{\nu_1}) / \ln(\nu_2/\nu_1)$. The structure of $\alpha_{97.5}^{225}$ and α_{225}^{405} are remarkably different, which will be interpreted in Section 3.

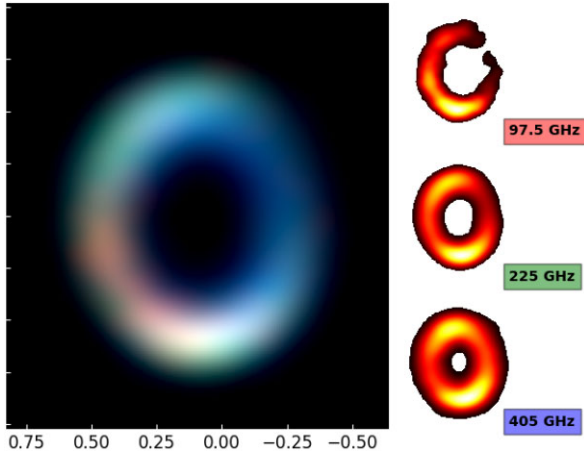


Figure 2. RGB image of the multifrequency observations of ISO-Oph 2A. Each image is masked below 10σ . **Red:** B3 continuum, restored with $r = 0.7$, with a beam of $0''.230 \times 0''.171$ along 90° . **Green:** B6 continuum, degraded to the B3 beam. **Blue:** B8 continuum, degraded to the B3 beam.

2.3 Astrometry of ISO-Oph 2B

The accuracy of the multifrequency alignment is $\lesssim 9$ mas, which is slightly better than the rule of thumb for the ALMA pointing accuracy, of about 1/10 of the clean beam (Remijan et al. 2019). In Table 2, we record the positions of ISO-Oph 2B, measured with elliptical Gaussian fits. The error budget is dominated by that of the Gaussian centroid, except for B6, for which we assign the nominal ALMA pointing accuracy.

It appears that ISO-Oph 2B is moving too fast, relative to ISO-Oph 2A, for Keplerian rotation. At their projected separation, of ~ 257 au, the Keplerian velocity for a $0.5 M_\odot$ system is $\sim 1.3 \text{ km s}^{-1}$, and only $\sim 0.8 \text{ km s}^{-1}$ after projection on to the plane of the sky with a disc inclination of 36° . However, the projected velocity comparing SB17 and B8 is $10.1 \pm 3.4 \text{ km s}^{-1}$, and is $6.0 \pm 2.5 \text{ km s}^{-1}$ when comparing B6 and B8. The difference between a bound orbit and circular orbit in the plane of the circumprimary disc are $\sim 2.7\sigma$ and $\sim 2.1\sigma$. A new epoch is required to conclude.

To further assess the possibility of an unbound trajectory for ISO-Oph 2B, we attempted to fit the five astrometric measurements with a bound orbit using ORBITIZE! (Blunt et al. 2020). We assumed a total mass of $0.58 \pm 0.15 M_\odot$ for the system ($0.5 M_\odot$ for A and $80 M_J$ for B; González-Ruilova et al. 2020), and a parallax of 7.449 ± 0.074 mas (Gaia Collaboration 2023). We considered two cases: no prior on the orbit, and tight Gaussian priors on the inclination and longitude of the ascending node for the orbital plane to match the plane of the circumprimary disc. In either cases, we drew 10 000 orbits with the OFTI algorithm and noted that the first epoch datum was $\sim 2\sigma$ discrepant from the closest orbit predictions at that epoch out of these $2 \times 10\,000$ samples. This provides another piece of evidence in favour of an unbound hyperbolic trajectory (i.e. a fly-by).

2.4 Photometry

Table 3 reports the integrated flux densities for each component of ISO-Oph 2. For ISO-Oph 2A, we used aperture photometry within a radius of $0''.8$, centred on the primary. For ISO-Oph 2B, we used the integrated flux density obtained with elliptical Gaussian fits.

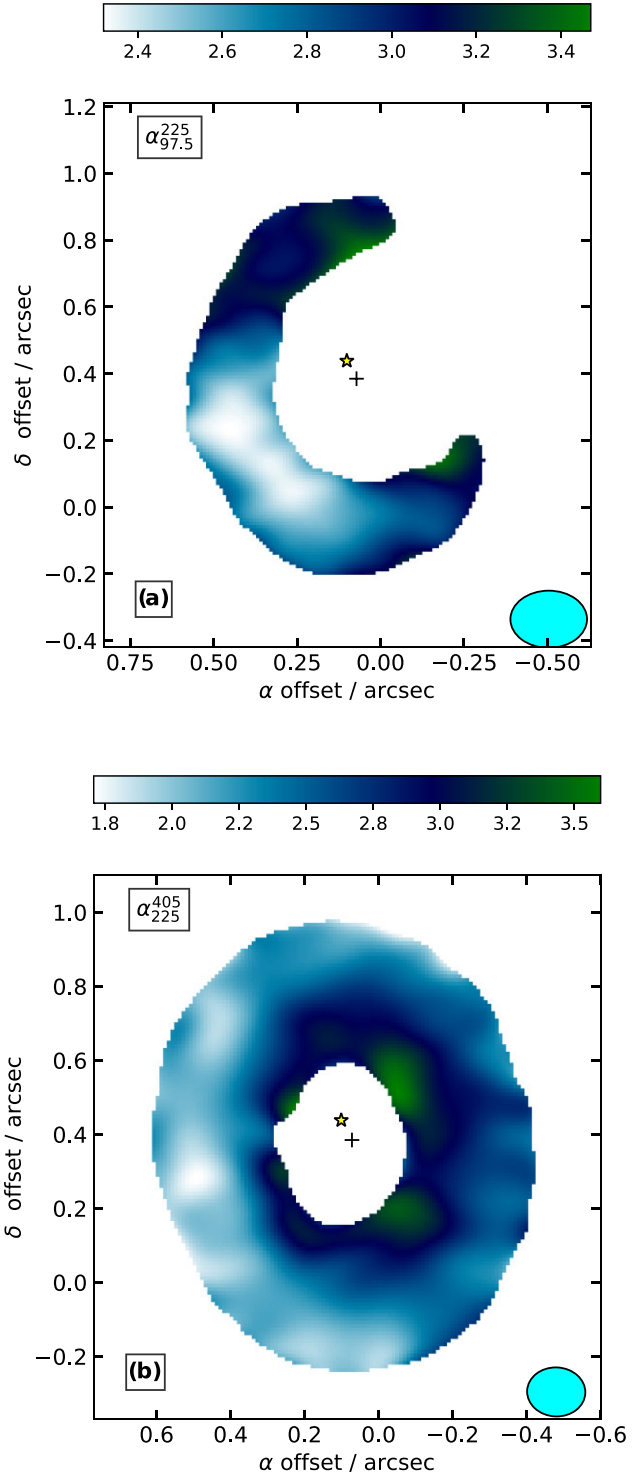


Figure 3. Intensity spectral index maps. (a) Spectral index between B3 and B6, at the resolution of B3 ($r = 0.7$). (b) Spectral index between B6 and B8, at the resolution of B8 ($r = 0$).

2.5 Disc orientation and stellar offset

The position of ISO-Oph 2A (from *GAIA* DR3, Gaia Collaboration 2023), corrected for proper motion, is at $\Delta\alpha = 0.101$ arcsec and $\Delta\delta = 0.438$ arcsec relative to the B6-LB19 phase centre. The errors on these coordinates are negligible relative to

Table 2. Multi-epoch astrometry for ISO-Oph 2B, relative to the phase centre for B6. In this system, the *Gaia* coordinates for the primary are $\Delta\alpha = 0.101$ arcsec and $\Delta\delta = 0.438$ arcsec.

Date	Data set	$\Delta\alpha^a$	$\Delta\delta^b$
2017-07-13	SB17	$0''.363 \pm 0''.023$	$-1''.349 \pm 0''.023$
2019-06-12	B6	$0''.399 \pm 0''.003$	$-1''.385 \pm 0''.003$
2021-07-27	B3	$0''.367 \pm 0''.028$	$-1''.341 \pm 0''.028$
2022-07-20	B4	$0''.423 \pm 0''.024$	$-1''.368 \pm 0''.024$
2022-08-04	B8	$0''.426 \pm 0''.013$	$-1''.393 \pm 0''.013$

^aOffset along RA, in arcsec. ^bOffset along Dec., in arcsec.

Table 3. Photometry of ISO-Oph 2 for each of the data sets presented in Fig. 1. We report flux densities in mJy. The errors do not include the systematic calibration uncertainty.

	B3	B4	B6	B8
ISO-Oph 2B	0.32 ± 0.03	0.50 ± 0.07	1.81 ± 0.01	7.3 ± 0.3
ISO-Oph 2A	6.05 ± 0.15	23.6 ± 0.3	85.5 ± 0.5	316 ± 2

the ALMA pointing accuracy for B6-LB19, which is ~ 3 mas. ISO-Oph 2A is remarkably offset from the ring centroid. Fig. 1 indicates the stellar position and the cavity centres for B6 and B8. We first centred each image on the primary, and then estimated the disc orientation and centre using the MPOLARMAPS package (described in Casassus et al. 2021). MPOLARMAPS min-

imizes the azimuthal scatter in radial profiles, which should yield the correct orientation parameters for an axially symmetric disc. Under this assumption, the best-fitting parameters for B6 are a position angle $PA = 2.42^{+0.45}_{-0.49}$ deg, an inclination of $i = 36.92^{+0.21}_{-0.24}$ deg, and disc centre relative to the stellar position: $\Delta\alpha = -0''.011 \pm 0''.001$, $\Delta\delta = -0''.062 \pm 0''.001$. The corresponding PA and i are consistent with those reported by González-Ruilova et al. (2020). For B4, we obtain $PA = 12.4^{+1.4}_{-1.4}$ deg, $i = 31.8^{+0.8}_{-0.9}$ deg, and $\Delta\alpha = -0''.015 \pm 0''.002$, $\Delta\delta = -0''.065 \pm 0''.002$, while for B8, $PA = 7.8^{+0.58}_{-0.65}$ deg, an inclination of $i = 36.62^{+0.41}_{-0.38}$ deg, and disc centre relative to the stellar position: $\Delta\alpha = -0''.001 \pm 0''.001$, $\Delta\delta = -0''.076 \pm 0''.001$.

In terms of their posterior distributions, the disc orientations inferred from MPOLARMAPS are well constrained (see Fig. 4). However, the above errors do not consider the systematics induced by the non-axial symmetry of the disc, which could well be intrinsically eccentric, hence the significant differences for each image. Still, a qualitatively large stellar offset, which can readily be seen by eye, is common to all three images. Such a large offset, of ~ 62 to ~ 76 mas, is rare in ringed systems with accurate optical/IR stellar astrometry. The associated eccentricity, for a $0''.43$ ring, ranges between 0.12 and 0.17. By comparison, the largest of such offsets, inferred from long-baseline continuum ALMA data, is 33 ± 3 mas in MWC 758 (Dong et al. 2018), and 12 ± 4 mas in HD 135344B (Casassus et al. 2021). The ring around IRS 48 also appears to be extremely eccentric, with $e \sim 0.27$ and an offset between the ring centroid and the central submm emission of $\sim 0''.15$ (Yang et al. 2023).

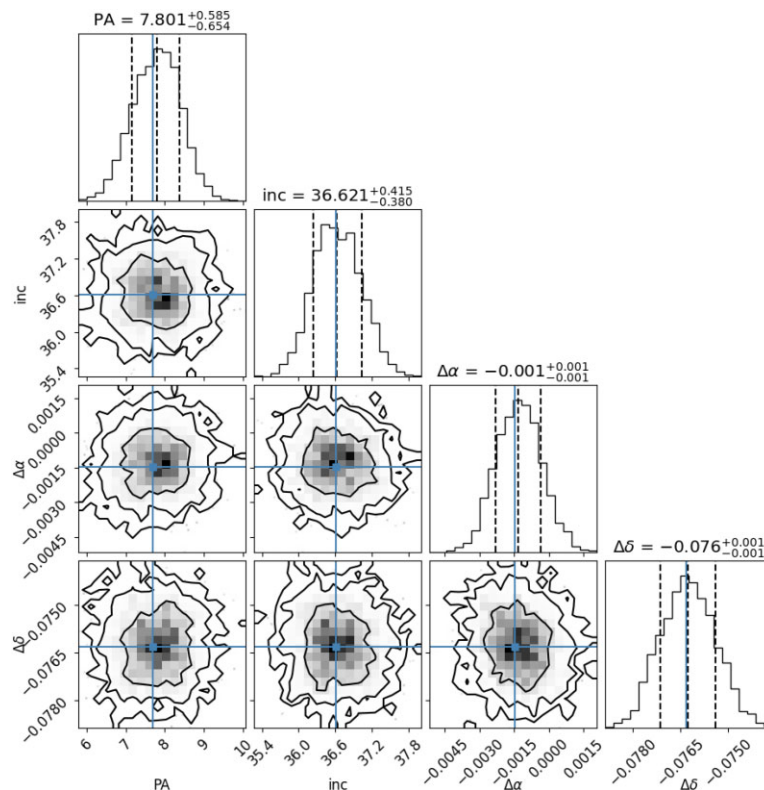


Figure 4. Corner plot from the optimization of the orientation parameters in ISO-Oph 2 A, using the B8 image with $r = 0$. The histograms plot the 1D probability density functions of the parameters indicated in titles, along with their median values and 1σ confidence intervals (i.e. at 16 per cent and 84 per cent), which are also shown by the vertical dashed lines. The contour plots show the marginalized 2D distributions (i.e. the 2D projection of the 8D posterior probability distribution), for the corresponding pairs of parameters. Contour levels are chosen at 0.68, 0.95, and 0.997.

3 ANALYSIS

3.1 Qualitative spectral trends

The RGB image in Fig. 2 is rich in structure, suggesting strong azimuthal variations in physical conditions. The low frequency spectral index $\alpha_{97.5}^{225}$ in Fig. 3 a reveals a clump of values around ~ 2.4 to the south-east, which could be the result of optically thin emission from a concentration of large grains, while the rest of the disc corresponds to smaller grains with $\alpha_{97.5}^{225} \sim 3.0$. In turn α_{225}^{405} in Fig. 3 b is more uniform with values of around 2.0 to the east, which could correspond to optically thick emission, while emission on the western side is more optically thin, with $\alpha_{225}^{405} \sim 3$. An optically thick region to the east could correspond to a lopsided disc, which would be consistent with the large grain clump in the dust trap hypothesis: grains with larger dimensionless stopping time (Stokes number), up to $S_t \lesssim 1$, pile up near the centre of the pressure maximum (e.g. Birnstiel, Dullemond & Pinilla 2013; Lyra & Lin 2013; Zhu & Stone 2014; Mittal & Chiang 2015; Baruteau & Zhu 2016; Casassus et al. 2019a).

3.2 Implementation of uniform-slab diagnostics in SLAB.CONTINUUM

We quantify the dust trapping scenario by interpreting the spectral variations in terms of dust properties averaged along the line of sight. We developed the package SLAB.CONTINUUM to model the emergent intensities from a uniform-slab, including isotropic scattering (in the Eddington approximation and with two-streams boundary conditions, following Miyake & Nakagawa 1993; D’Alessio, Calvet & Hartmann 2001; Sierra, Lizano & Barge 2017; Casassus et al. 2019a; Sierra et al. 2019):

$$I_v^m(\tau_v, \mu) = B_v(T) \left[1 - \exp\left(-\frac{\tau_v}{\mu}\right) + \omega_v \mathcal{F}_v \right], \quad (1)$$

where

$$\mathcal{F}_v = \frac{1}{(\sqrt{1-\omega_v}-1)\exp(-\sqrt{3(1-\omega_v)}\tau_v) - (\sqrt{1-\omega_v}+1)} \times \left\{ \frac{1 - \exp\left[-\frac{(\sqrt{3(1-\omega_v)} + \mu^{-1})\tau_v}{\sqrt{3(1-\omega_v)}\mu + 1}\right]}{\sqrt{3(1-\omega_v)}\mu + 1} + \frac{\exp\left(-\frac{\tau_v}{\mu}\right) - \exp(-\sqrt{3(1-\omega_v)}\tau_v)}{\sqrt{3(1-\omega_v)}\mu - 1} \right\}, \quad (2)$$

$\omega = \frac{\kappa^{\text{sca}}}{\kappa^{\text{abs}} + \kappa^{\text{sca}}}$ is the dust albedo, $\tau_v \equiv \Sigma_g \kappa_v$, and $\kappa_v = \kappa^{\text{abs}} + \kappa^{\text{sca}}$. The angle of incidence, $\mu = \cos(i)$, was set to 1 for simplicity, thus reducing equation (2) to equations (24) and (25) of Sierra et al. (2019).

The size-averaged dust opacities κ_v^{abs} and κ_v^{sca} were computed using routines from the DSHARP_OPAC package,² described in Birnstiel et al. (2018), and with their default effective optical constants (fig. 2 in Birnstiel et al. 2018, i.e. ‘DSHARP’ opacities). Forward scattering was accounted for by correcting the scattering opacity κ_v^{sca} to $(1 - g_v)\kappa_v^{\text{sca}}$, where g_v is the Henyey–Greenstein anisotropy parameter.

For a power-law distribution of dust grain sizes, with a single dust composition, and for a fixed gas-to-dust mass ratio (taken here to be 100), the free parameters for any given line of sight are the total

mass column density Σ_g , the maximum grain size a_{max} , the dust size exponent q , and the dust temperature T_d . We fit the spectral energy distribution (SED) for each line of sight, with N independent frequency points $\{I_{\nu_i}\}_{i=1}^N$, by minimizing

$$\chi^2 = \sum_i \frac{(I_{\nu_i} - I_{\nu_i}^m)^2}{\sigma_i^2}, \quad (3)$$

where the weights $\{1/\sigma_i^2\}$ are approximated as the root-mean-square dispersion for each residual image,³ including the flux calibration error in quadrature. The flux calibration accuracy was taken to be 5 per cent in B3, 5 per cent in B4, 5 per cent in B6, and 10 per cent in B8.

The posterior distributions were calculated with a Markov chain Monte Carlo ensemble sampler (Goodman & Weare 2010). We used the EMCEE package (Foreman-Mackey et al. 2013), with 1000 iterations, a burn-in of 800, and 10 walkers per free parameter. Except for q , we varied the logarithm of each parameter, with flat priors, and across wide domains in parameter space: $0 < \log(T_d/\text{K}) < 3$, $-5 < \log(\Sigma_g/g \text{ cm}^{-2}) < 3$ and $-3 < \log(a_{\text{max}}/\text{cm}) < 10$, and $-3.99 < q < -2$. The SLAB.CONTINUUM package optionally runs a final optimization with the Powell variant of the conjugate-gradient minimization algorithm, using the maximum-likelihood parameters obtained with EMCEE. Rather than calculate size-averaged opacities for all sampled values of a_{max} and q , we first computed opacity grids in a_{max} and q , at each of the frequencies $\{\nu_i\}_{i=1}^N$, and used bilinear interpolation.

3.3 Application of SLAB.CONTINUUM to ISO-Oph 2A

Initial trials including B4 resulted in strong biases due to beam dilution, when the beam is much larger than the structures (see below). We therefore discarded B4 from the spectral fits. With $N = 3$ independent spectral points, we may optimize only up to three parameters. For the present application of SLAB.CONTINUUM, we thus chose to fix $q = -3.5$, i.e. as in the standard interstellar medium size distribution (Mathis, Rumpl & Nordsieck 1977).

Before running the optimization on all lines of sight, and in order to reduce the load on computer resources, we resampled each image $\{I_{\nu_i}\}_{i=1}^N$ into coarser pixels (in synthesis imaging the pixel size is usually chosen to be around 1/10 of the natural weights clean beam). We additionally set an intensity mask at 10σ in B6.

The coarsest data point is B3, and thus the full set of frequency points was degraded to the B3 beam with $r = 0$. The result is summarized in Fig. 5, where we see that the inferred dust parameters bear fairly large uncertainties, especially to the west, where the disc is faintest in B3. Example SEDs, for the lines of sight towards the intensity extrema in B6 and along the eastern side of the ring, are shown in Fig. 6. A corner plot for the posterior probability distributions towards the peak is shown in Fig. 7. We see that a_{max} is poorly constrained, which we tentatively interpret in terms of two dominant effects. First, towards the minimum in B4, to the west of the ring, the solutions for large grains, $\log(a_{\text{max}}/\text{cm}) > 0.8$, correspond to optically thin emission at all frequencies, where intensities are proportional to optical depth, $I_{\nu} \propto T_d \tau_v$. Since $\tau_v \propto \Sigma_g$, the lack of an additional point in the optically thick regime prevents lifting the $T_d - \Sigma_g$ degeneracy. Second, even with an optically thick point with which to set T_d , for grains that are larger than the wavelength, increasing grains larger have lower opacity κ_v , so

²https://github.com/birnstiel/dsharp_opac

³The dirty map of the residual visibilities.

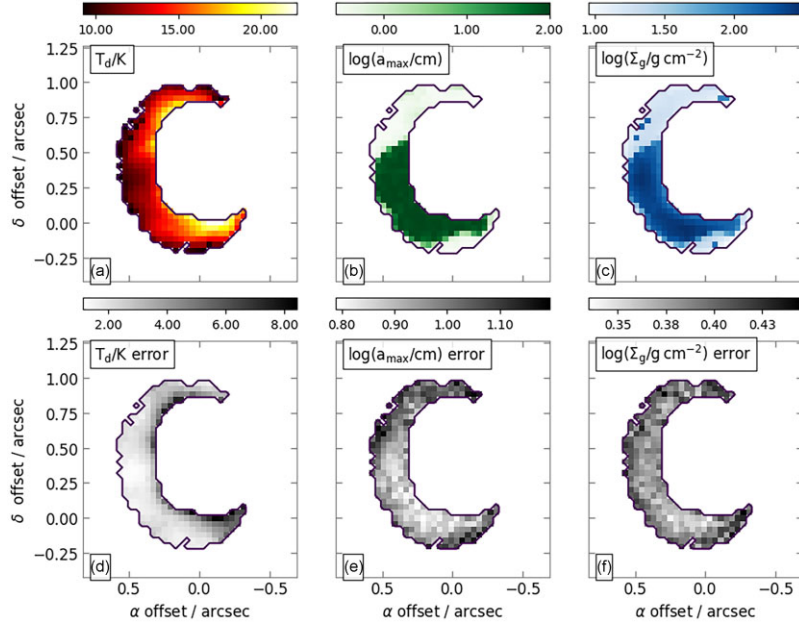


Figure 5. Dust parameters for each line of sight from the uniform-slab optimizations of T_d , a_{\max} , and Σ_g , and constrained with the B3, B6, and B8 all degraded to the B3 beam with $r = 0.7$. The black contours outline an error mask on $\log_{10}(T_d)$, set to 0.2. (a) Maximum-likelihood T_d . (b) Maximum-likelihood $\log_{10}(a_{\max})$. (c) Maximum-likelihood $\log_{10}(\Sigma_g)$. (d) 1σ uncertainty on T_d , approximated as $\sigma(T_d) = \ln(10)T_d\sigma(\log(T_d))$, where $\sigma(\log(T_d))$ is estimated with the average of the upwards and downwards 34 per cent confidence intervals around the median. (e) 1σ uncertainty on $\log_{10}(a_{\max})$. (f) 1σ uncertainty on $\log_{10}(\Sigma_g)$. The blue lines correspond to the maximum-likelihood values.

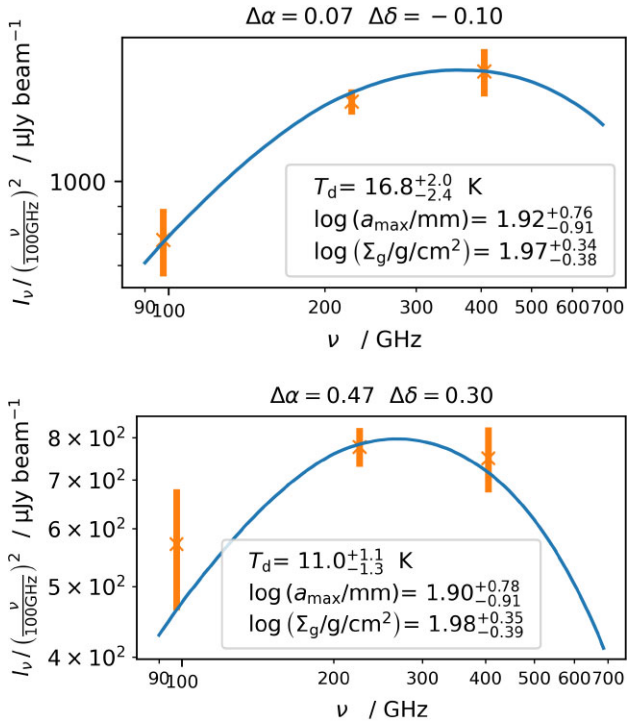


Figure 6. SED and best-fitting uniform-slab model for two example lines of sight. The direction of each line of sight is given as offset from the phase centres, in arcsec, on top of each plot. Top: Line of sight towards the peak B6 intensity. Bottom: Line of sight towards the minimum in B6 intensity along the eastern side of the ring.

that a given optical depth may result from arbitrarily large grains $\tau_v = \kappa_v \Sigma_g$, leading to the $a_{\max} - \Sigma_g$ degeneracy (e.g. Sierra et al. 2021). We set the maximum grain size to 100 cm, which corresponds to the maximum size in the default opacities from Birnstiel et al. (2018).

3.4 Incorporation of a beam filling factor

Beam dilution, or the reduction of specific intensities in sources that do not fill the clean beam, is strong in the coarse B3 beam, even with $r = 0$. This also translates into a reduction in brightness temperature, which reaches only ~ 5 K in B3 and ~ 10 K in the finer beam of B6 (in ISO-Oph 2A, Fig. B1). Without a beam filling factor among the free parameters, the uniform-slab model is a poor approximation. For instance, in the case of T_d and optically thick emission, beam dilution would lower the brightness temperature, but the spectral indices would still correspond to the undiluted blackbody emission. Similarly, a_{\max} determines the spectral indices and opacity, which may not match the observed intensities if they are diluted. A question arises on the impact of beam dilution on the inferred physical parameters.

The B6 data set is well sampled, and can be used to estimate the filling factor in B6, by comparing the B6 map in native resolution (I_{B6}) with its smoothed version (I_{B6}^s), $f = I_{B6}^s/I_{B6}$, with an upper limit of 1. The resulting map is shown in Fig. 8. We use this map to scale the multifrequency intensities; i.e. the corrected intensities are $I_v^c = I_v/f$. The corresponding dust properties are shown in Fig. 9, with example SEDs in Fig. 10. It is interesting to note that χ^2 , as given by equation (C1), is reduced from 1.1 to 0.11 with the incorporation of the filling factor for the line of sight towards the peak B6 intensity. This probably reflects the improved model in B6. However, there is no appreciable difference for the line of sight towards the minimum

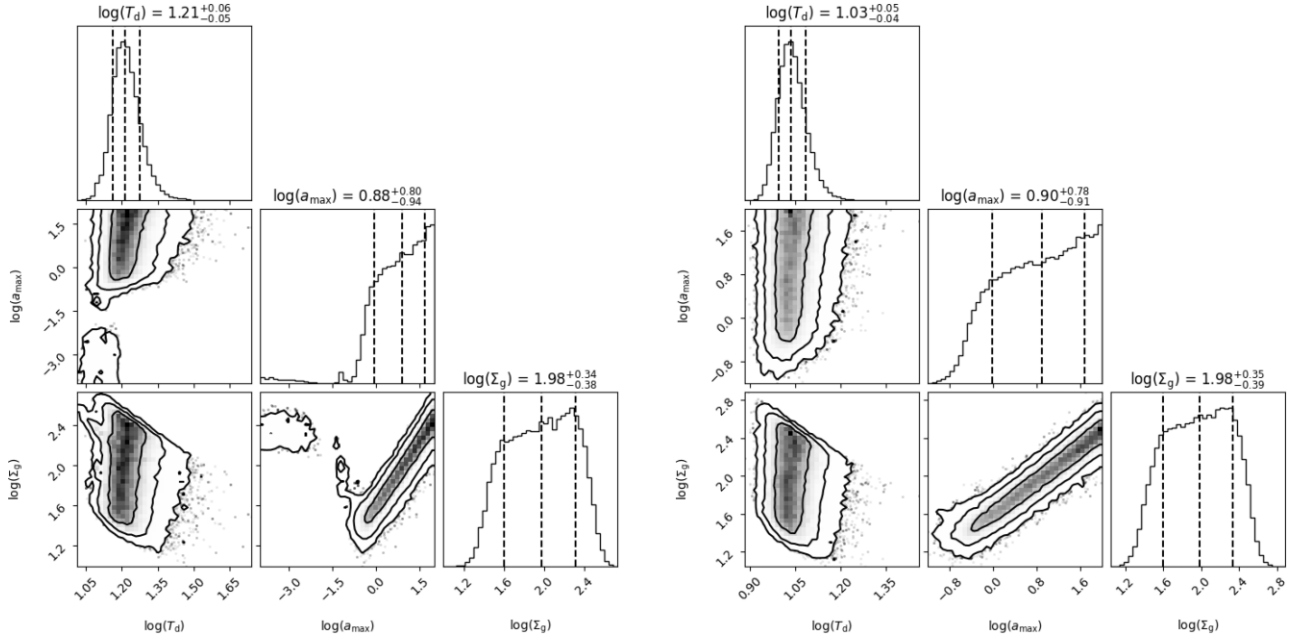


Figure 7. Annotations follow from Fig. 4. Left: Corner plot for the dust parameters towards the peak B6 intensity, corresponding to Fig. 6 (top). Right: Corner plot for the dust parameters towards the minimum B6 intensity along the eastern ring, and corresponding to Fig. 6 (bottom).

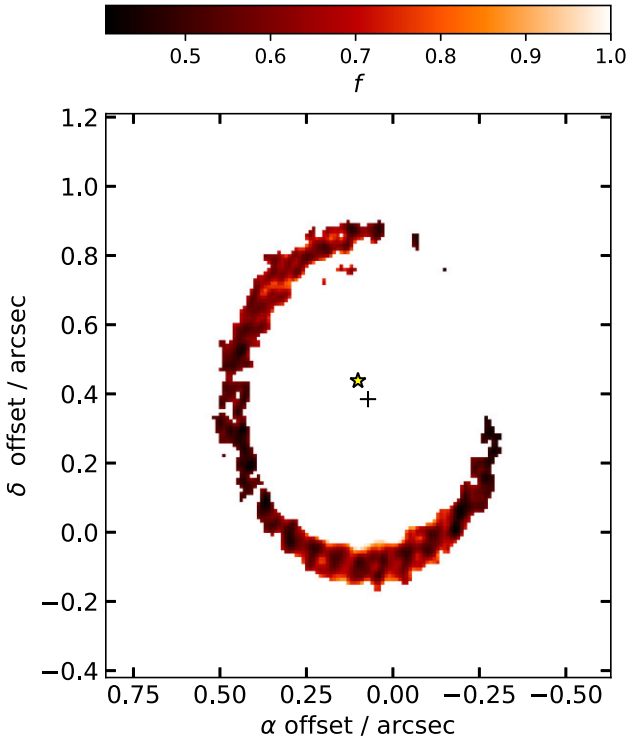


Figure 8. Beam filling factor inferred from the B6 data set.

B6 intensity (to the east of the ring), where χ^2 increases from 1.1 to 1.2 with the inclusion of a filling factor.

3.5 Fixing a_{\max}

In Fig. 11, we explore a fit with only two free parameters, i.e. T_d and Σ_g . In order to reach the optically thick limit close to B8, and thus

lift the $T_d - \Sigma_g$ degeneracy, we set $a_{\max} = 0.01$ cm. This choice yields well-constrained posteriors for T_d and Σ_g . Fixing $a_{\max} \gtrsim 1$ cm results in optically thin emission to the west, and large errors on T_d . However, in the east the morphologies of T_d and Σ_g are very similar in both cases.

3.6 Discussion

An interesting result of the present estimates of physical conditions is the significant variations in T_d along the ring, and especially along the eastern arc. In the fits including B3, the minimum along the ring is $\log(T_d/K) = 1.04 \pm 0.04$, while T_d reaches $\log(T_d/K) = 1.32 \pm 0.08$ to the north and south. The fits to the B6 and B8 data reach higher T_d , as expected since beam dilution is reduced, and cover all azimuth. In Fig. 12, we extracted the azimuthal profile for T_d , for which we adopted the orientation from the B8 estimates, i.e. PA = 7.8 deg and $i = 36.6$ deg. The variations in T_d are quite significant, and reach $\log(T_d/K) = 1.175 \pm 0.017$ in the north, and $\log(T_d/K) = 1.210 \pm 0.015$ in the south, with a minimum towards the east at $\log(T_d/K) = 1.036 \pm 0.014$, which represents over 8σ .

Interestingly, the PA on the sky of the line joining the two peaks in Fig. 12(b) is 193.5 deg, and is remarkably close to the direction of HD 147889, which is at 210.5 deg. The azimuthal temperature modulation might thus result from a variation of the angle of incidence of radiation coming from HD 147889. Such external irradiation would hit the southern edge of the disc almost edge-on, and since the disc is flared, the region where it would reach the disc surface at closest to normal incidence is to the north. The small difference between the PA joining the two temperature maxima might be due to biases in our estimate of the dust temperature, since here we kept the dust grain size fixed at a small value that ensures that B8 is in the optically thick regime. Another interesting possibility is that, if the disc is retrograde (rotating clockwise), then the small angular shift could be due to the thermal lag discussed in Casassus et al. (2019b).

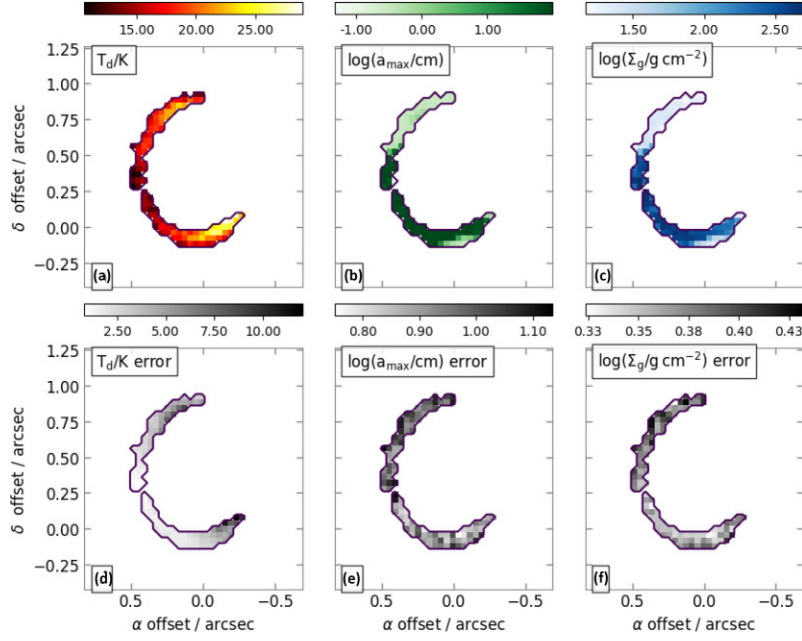


Figure 9. Dust parameters for each line of sight from the uniform-slab optimizations of T_d , a_{\max} , and Σ_g , including a filling factor, and constrained with the B3, B6, and B8 all degraded to the B3 beam with $r = 0.7$. Annotations follow from Fig. 5.

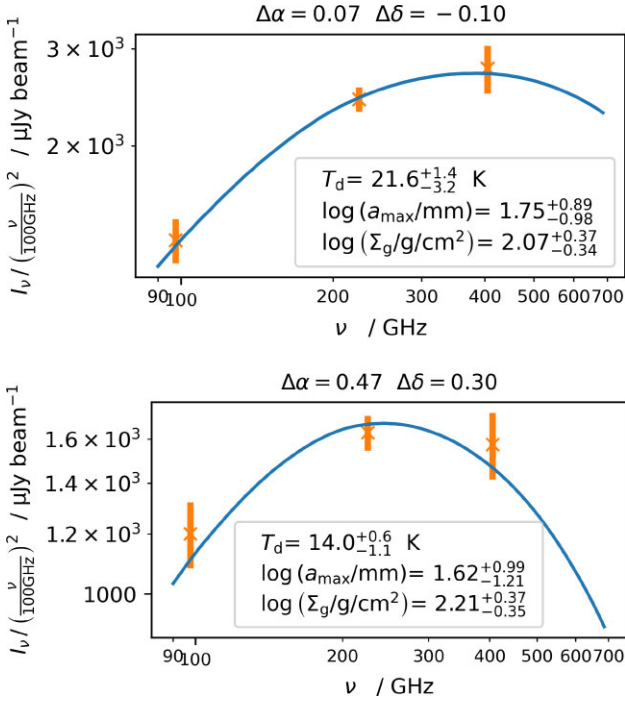


Figure 10. SED and best-fitting uniform-slab model for two example lines of sight, with a filling factor. Annotations follow from Fig. 6.

4 CONCLUSIONS

We report new ALMA continuum observations of the ISO-Oph 2 binary, at 97, 145, and 405 GHz, that complement existing 225 GHz data. A novel strategy for the alignment of multifrequency data, acquired with broadly different angular resolutions, allowed us to reach the following conclusions:

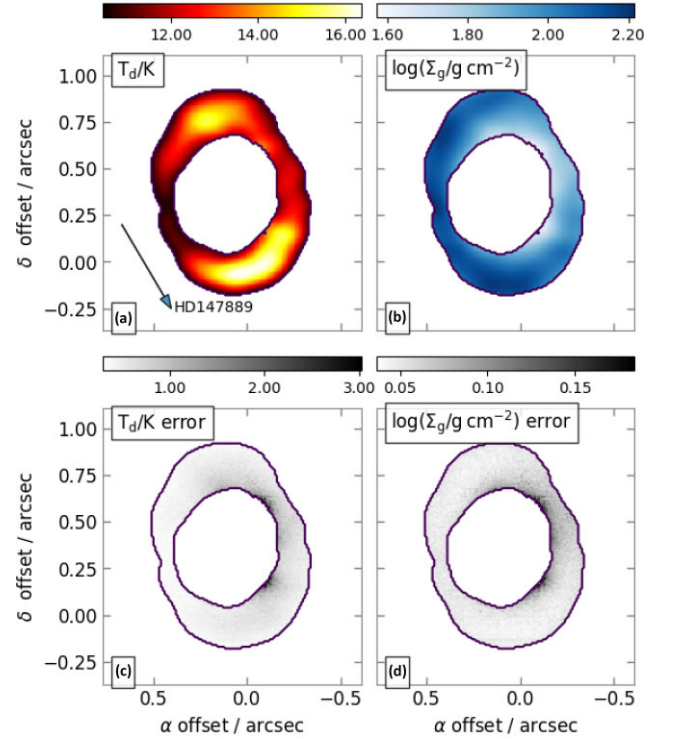


Figure 11. Dust parameters for each line of sight from the uniform-slab optimizations of T_d and Σ_g , constrained with the B8 and B6 data, degraded to the B8 beam with $r = 0$. The black contours outline an intensity mask, set to 20σ in B8. (a) Maximum-likelihood T_d . The arrow points to the direction of HD 147889. (b) Maximum-likelihood $\log_{10}(\Sigma_g)$. (c) 1σ uncertainty on T_d , approximated as $\sigma(T_d) = \ln(10)T_d\sigma[\log(T_d)]$. (d) 1σ uncertainty on $\log_{10}(\Sigma_g)$.

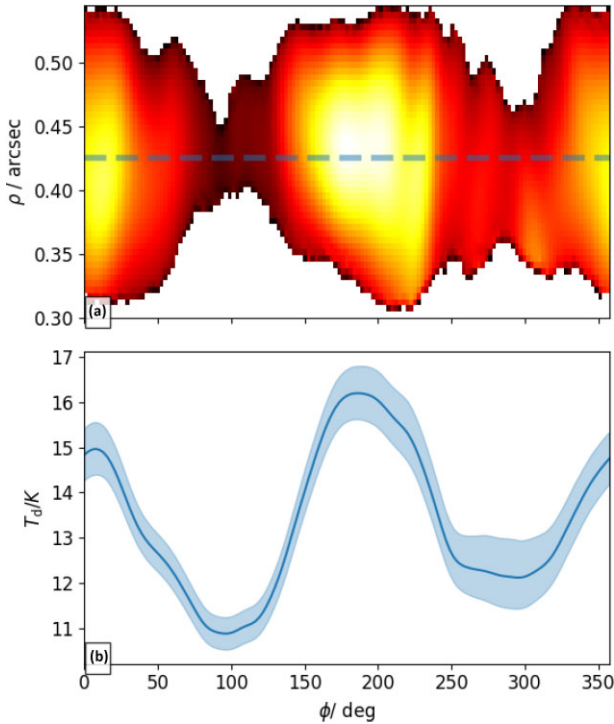


Figure 12. Polar expansion of the temperature map from Fig. 11(a), shown with the same colour scale, and its azimuthal profile, as extracted at a radius $\rho = 0.425$ arcsec. The shaded area corresponds to the region enclosed by the 1σ uncertainties (its total vertical extent is 2σ). The extraction radius is indicated as a dashed line in the top panel.

(i) The offset of ISO-Oph2A relative to the centroid of the circumprimary disc is remarkably large, 62–76 mas depending on the image (Fig. 1). Such a large offset points at dynamical interactions, either with ISO-Oph 2B or with other massive bodies inside the ring of ISO-Oph 2A.

(ii) The multifrequency data reveal strong morphological variations with frequency in ISO-Oph2A (Fig. 2). We linked these variations to the underlying physical conditions by modelling the data with uniform-slab intensities (Figs 5 and 11).

(iii) Surprisingly, the dust temperature varies strongly in azimuth (Fig. 12), and roughly traces a second harmonic with four nodes. The PA joining the two peaks, each to the north and south of the disc, is aligned in the direction towards HD 147889 within 10 deg. Such an azimuthal temperature modulation is in qualitative agreement with external irradiation as the dominant heat source.

(iv) As in several other discs, we find indications for a lopsided disc, where the dust column density is shaped into a crescent. The maximum grain size appears to coincide with the peak column density, as expected for aerodynamic dust trapping (Fig. 5).

(v) The multi-epoch astrometry of the binary is only marginally consistent with a bound orbit, in support (but at $\sim 2\sigma$) of the view that the binary is in fact a fly-by.

The binary discs of ISO-Oph2 are interesting laboratories for the impact of environmental effects on disc structure, with strong dynamical perturbations on the circumprimary ring. The temperature structure of this ring is also suggestive of heating by external irradiation, probably from HD 147889. This possibility will be considered in a companion article on radiative transfer modelling of external irradiation in ISO-Oph 2.

ACKNOWLEDGEMENTS

We thank the two referees (an anonymous referee and Prof. Takayuki Muto) for their constructive comments. SC, LC, and MC acknowledge support from Agencia Nacional de Investigación y Desarrollo de Chile (ANID) given by FONDECYT regular grants 1211496, 1211656, ANID PFCHA/DOCTORADO BECAS CHILE/2018-72190574, ANID project Data Observatory Foundation DO210001, and ANID – Millennium Science Initiative Program – Center Code NCN2021 080. AR has been supported by the UK Science and Technology research Council (STFC) via the consolidated grant ST/W000997/1 and by the European Union’s Horizon 2020 research and innovation programme under the Marie Skłodowska-Curie grant agreement no. 823823 (RISE DUSTBUSTERS project). VC acknowledges a postdoctoral fellowship from the Belgian F.R.S.-FNRS. TB acknowledges financial support from the FONDECYT postdoctorado project number 3230470. AR-J acknowledges funding from ANID-Subdirección de Capital Humano/Doctorado Nacional/2022-21221841. This paper makes use of the following ALMA data: ADS/JAO.ALMA#2022.1.01734.S, #2021.1.00378.S, 2019.1.01111.S, and #2018.1.00028.S. ALMA is a partnership of ESO (representing its member states), NSF (USA), and NINS (Japan), together with NRC (Canada), MOST and ASIAA (Taiwan), and KASI (Republic of Korea), in cooperation with the Republic of Chile. The Joint ALMA Observatory is operated by ESO, AUI/NRAO, and NAOJ.

DATA AVAILABILITY

The reduced ALMA data presented in this article are available upon reasonable request to the corresponding author. The original or else non-standard software packages underlying the analysis are available at the following URLs: MPOLARMAPS (<https://github.com/simoncasassus/MPolarMaps>, Casassus et al. 2021), UVMEM (<https://github.com/miguelcarcamov/gpvmem>; Cárcamo et al. 2018), PYRALYSIS (<https://gitlab.com/clirai/pyralysis>), VISALIGN (<https://github.com/simoncasassus/VisAlign>), and SNOW (<https://github.com/miguelcarcamov/snow>).

REFERENCES

- Andrews S. M., Wilner D. J., Hughes A. M., Qi C., Dullemond C. P., 2009, *ApJ*, 700, 1502
 Andrews S. M., Wilner D. J., Hughes A. M., Qi C., Dullemond C. P., 2010, *ApJ*, 723, 1241
 Ansdell M. et al., 2016, *ApJ*, 828, 46
 Ansdell M. et al., 2018, *ApJ*, 859, 21
 Barenfeld S. A., Carpenter J. M., Ricci L., Isella A., 2016, *ApJ*, 827, 142
 Baruteau C., Zhu Z., 2016, *MNRAS*, 458, 3927
 Benisty M. et al., 2021, *ApJ*, 916, L2
 Birnstiel T., Dullemond C. P., Pinilla P., 2013, *A&A*, 550, L8
 Birnstiel T. et al., 2018, *ApJ*, 869, L45
 Blunt S. et al., 2020, *AJ*, 159, 89
 Cárcamo M., Román P. E., Casassus S., Moral V., Rannou F. R., 2018, *Astron. Comput.*, 22, 16
 Casassus S., Cárcamo M., 2022, *MNRAS*, 513, 5790
 Casassus S., Cabrera G. F., Förster F., Pearson T. J., Readhead A. C. S., Dickinson C., 2006, *ApJ*, 639, 951
 Casassus S. et al., 2008, *MNRAS*, 391, 1075
 Casassus S. et al., 2019a, *MNRAS*, 483, 3278
 Casassus S., Pérez S., Osses A., Marino S., 2019b, *MNRAS*, 486, L58
 Casassus S. et al., 2021, *MNRAS*, 507, 3789

Cieza L. A. et al., 2019, *MNRAS*, 482, 698
 Cieza L. A. et al., 2021, *MNRAS*, 501, 2934
 Cox E. G. et al., 2017, *ApJ*, 851, 83
 Cuello N., Ménard F., Price D. J., 2023, *Eur. Phys. J. Plus*, 138, 11
 Czekala I. et al., 2021, *ApJS*, 257, 2
 D'Alessio P., Calvet N., Hartmann L., 2001, *ApJ*, 553, 321
 Dong R. et al., 2018, *ApJ*, 860, 124
 Dong R. et al., 2022, *Nat. Astron.*, 6, 331
 Eisner J. A. et al., 2018, *ApJ*, 860, 77
 Foreman-Mackey D., Hogg D. W., Lang D., Goodman J., 2013, *PASP*, 125, 306
 Gaia Collaboration, 2023, *A&A*, 674, A1
 González-Ruilova C. et al., 2020, *ApJ*, 902, L33
 Goodman J., Weare J., 2010, *Commun. Appl. Math. Comput. Sci.*, 5, 65
 Guilloteau S., Dutrey A., Piétu V., Boehler Y., 2011, *A&A*, 529, A105
 Haworth T. J., 2021, *MNRAS*, 503, 4172
 Isella A., Carpenter J. M., Sargent A. I., 2009, *ApJ*, 701, 260
 Jorsater S., van Moorsel G. A., 1995, *AJ*, 110, 2037
 Long F. et al., 2018, *ApJ*, 869, 17
 Long F. et al., 2019, *ApJ*, 882, 49
 Longmore S. N., Chevance M., Kruijssen J. M. D., 2021, *ApJ*, 911, L16
 Lyra W., Lin M.-K., 2013, *ApJ*, 775, 17
 Mann R. K. et al., 2014, *ApJ*, 784, 82
 Mathis J. S., Ruml W., Nordsieck K. H., 1977, *ApJ*, 217, 425
 Mittal T., Chiang E., 2015, *ApJ*, 798, L25
 Miyake K., Nakagawa Y., 1993, *Icarus*, 106, 20
 O'dell C. R., Wen Z., 1994, *ApJ*, 436, 194
 Pascucci I. et al., 2016, *ApJ*, 831, 125
 Remijan A. et al., 2019, ALMA Technical Handbook, ALMA Doc. 7.3, ver. 1.1
 Ruíz-Rodríguez D. et al., 2018, *MNRAS*, 478, 3674
 Shuai L., Ren B. B., Dong R., Zhou X., Pueyo L., De Rosa R. J., Fang T., Mawet D., 2022, *ApJS*, 263, 31
 Sierra A., Lizano S., Barge P., 2017, *ApJ*, 850, 115
 Sierra A., Lizano S., Macías E., Carrasco-González C., Osorio M., Flock M., 2019, *ApJ*, 876, 7
 Sierra A. et al., 2021, *ApJS*, 257, 14
 Villenave M. et al., 2021, *A&A*, 653, A46
 Wilhelm M. J. C., Portegies Zwart S., Cournoyer-Cloutier C., Lewis S. C., Polak B., Tran A., Mac Low M.-M., 2023, *MNRAS*, 520, 5331
 Williams J. P., Cieza L., Hales A., Ansdell M., Ruiz-Rodríguez D., Casassus S., Perez S., Zurlo A., 2019, *ApJ*, 875, L9
 Winter A. J., Haworth T. J., 2022, *Eur. Phys. J. Plus*, 137, 1132
 Winter A. J., Kruijssen J. M. D., Longmore S. N., Chevance M., 2020, *Nature*, 586, 528
 Yang H., Fernández-López M., Li Z.-Y., Stephens I. W., Looney L. W., Lin Z.-Y. D., Harrison R., 2023, *ApJ*, 948, L2

Zhu Z., Stone J. M., 2014, *ApJ*, 795, 53
 Zurlo A. et al., 2020, *MNRAS*, 496, 5089
 Zurlo A. et al., 2021, *MNRAS*, 501, 2305

APPENDIX A: ON THE JvM CORRECTION

The so-called JvM correction (Jorsater & van Moorsel 1995; Czekala et al. 2021) is thought to improve the dynamic range of images restored from radio-interferometric data. However, here we did not apply the JvM correction, because the resulting improvement is due to a spurious down-scaling of the image residuals, as shown in Casassus & Cárcamo (2022). Despite the proof, since its publication several workers have kept on applying the JvM correction, which leads us to believe that perhaps the arguments presented in Casassus & Cárcamo (2022) may not be clear enough. Here, we give more details on the argumentation that defines the units of the dirty map in interferometric image reconstruction.

As summarized in Appendix A of Casassus & Cárcamo (2022, equation A2), the restored image is obtained by adding the dirty map R_D of the visibility residuals with the model image I_m , after convolution with the clean beam g_b :

$$I_R = I_m * g_b + R_D. \quad (\text{A1})$$

Both the convolved model image and dirty residuals must of course bear the same units. Casassus & Cárcamo (2022) proposed to tie these units to the case of a point source at the phase centre, where the flux of the point source and its uncertainty can be inferred from parametric modelling of the visibility data (e.g. their equations A11 and A12). They matched this uncertainty to the thermal uncertainty on the specific intensity in the dirty map at the phase centre (their equations A13 and A14).

However, Casassus & Cárcamo (2022) did not explain the relationship between the general expression for the dirty map I_D (originally in equation A9) and that of the residuals R_D in equation (A1) above. Here, we clarify that, for the test case of a point source at the phase centre, the uncertainties on I_R stem from the thermal noise in R_D , since the model of the source is known. The dirty map R_D is itself an application of the general formula for I_D to the residual visibilities of the parametric fit. These residuals should contain only noise in this idealized test case.

APPENDIX B: BRIGHTNESS TEMPERATURE MAPS

Fig. B1 includes a summary of the self-calibrated and aligned data, as in Fig. 1, but in brightness temperature.

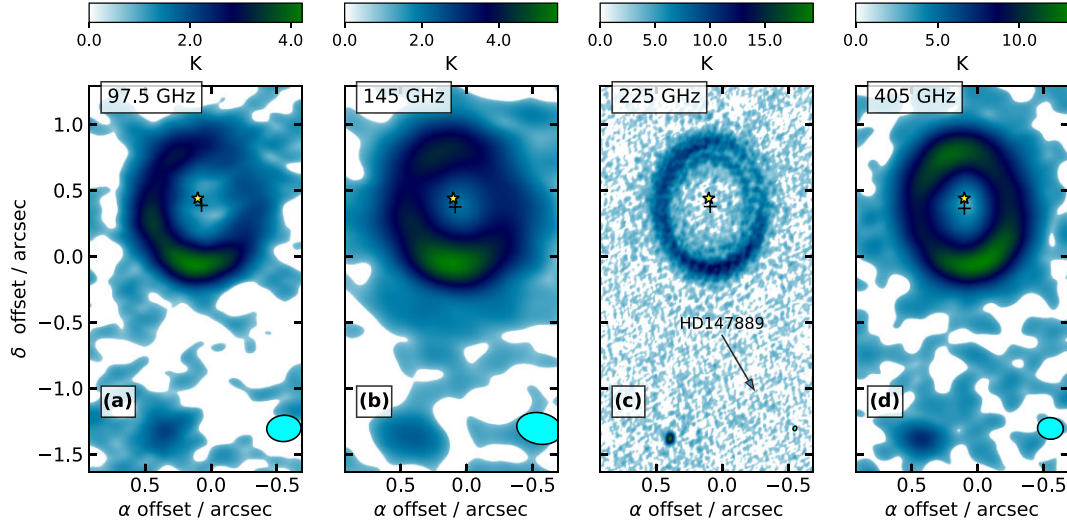


Figure B1. Same as Fig. 1, but for brightness temperature maps. The images have been clipped at 0 K.

APPENDIX C: FIGURE OF MERIT FOR THE ALIGNMENT OF VISIBILITY DATA SETS

The alignment of the multifrequency visibility data was performed with the VISALIGN⁴ package, described in Casassus & Cárcamo (2022). However, here we improved VISALIGN with an adjustment to the figure of merit, as the least-squares formula associated with the alignment of two visibility data sets, i.e. equation 1 in Casassus & Cárcamo (2022), was biased in the choice of reference data set. In this appendix, we revisit the least-squares figure of merit used to perform the alignment of two visibility data sets, i.e. equation 1 in Casassus & Cárcamo (2022), which we reproduce here for clarity:

$$\chi_{\text{align}}^2(\alpha_R, \delta\vec{x}) = \sum_{k=1}^N W_k^{\text{align}} \|\tilde{V}_k^L - \tilde{V}_k^{Lm}\|^2, \quad (\text{C1})$$

where

$$\tilde{V}_k^{Lm} = \alpha_R e^{i2\pi \delta\vec{x} \cdot \vec{u}_k} \tilde{V}_k^S, \quad (\text{C2})$$

and

$$W_k^{\text{align}} = \frac{W_k^S W_k^L}{W_k^S + W_k^L}. \quad (\text{C3})$$

With such weights W_k , the minimization of χ_{align}^2 in equation (C1) is not symmetric in the choice of reference data set for the alignment of the two visibility data sets $\{\tilde{V}_k^S\}_{k=1}^N$ and $\{\tilde{V}_k^L\}_{k=1}^N$. In other words, aligning \tilde{V}^S to \tilde{V}^L does not yield the opposite shift and reciprocal flux correction as aligning \tilde{V}^L to \tilde{V}^S . A symmetric expression, now implemented in the VISALIGN⁵ package, is obtained by replacing the weights with:

$$W_k^{\text{align}} = \frac{W_k^S W_k^L}{W_k^S + \alpha_R^2 W_k^L}. \quad (\text{C4})$$

We confirmed that with this modification the alignment is now independent on the choice of reference data set, in the sense that the astrometric shifts are opposite and the flux scale factors are reciprocal (down to the round-off numerical accuracy).

⁴<https://github.com/simoncasassus/VisAlign>

⁵<https://github.com/simoncasassus/VisAlign>

The impact on the corresponding flux scale factors and astrometric shifts is small (~ 5 per cent – 10 per cent). For example, following the nomenclature of Benisty et al. (2021) for the each visibility data set, the updated flux scale correction factors are $\alpha_R = 0.817 \pm 0.003$ to match SB16 to LB19, and $\alpha_R = 0.837 \pm 0.002$ to match IB17 and LB19.

Another consequence is that the shifts are no longer sensitive to the choice of uv -range, and depend only on the choice of uv -plane cell size for gridding, Δu . We checked that the shifts are all consistent within the errors for widely different choices of Δu , ranging from the antenna diameter to the minimum baseline length.

APPENDIX D: UPDATE TO THE MULTI-EPOCH RADIO-CONTINUUM IMAGING OF PDS 70

The impact of the revised alignment on the corresponding flux scale factors and astrometric shifts, although small (~ 5 per cent – 10 per cent), affects the multi-epoch analysis of PDS 70 reported in Casassus & Cárcamo (2022). Here, we update the resulting images. All the conclusions from Casassus & Cárcamo (2022) hold, but the variability of PDS 70c is more significant.

As in Casassus & Cárcamo (2022), we self-calibrated each data set individually before concatenation. Self-calibration was performed automatically with the OOSELFCAL package, which we re-baptized to ‘Self-calibratiON Object-oriented frameWork’, i.e. SNOW.⁶ A consequence of the updated figure of merit is that the PSNRs for the concatenated data sets are already close to the values obtained after joint self-calibration.

The LB19 data set was used as reference for the alignment of the multi-epoch data. However, the 2020 *Gaia* coordinates (DR 3, *Gaia* Collaboration 2023) for PDS 70 are offset by 9.2 mas relative to the LB19 phase centre, by 8.2 mas in RA and -4.2 mas in Dec. This shift is larger than the nominal pointing accuracy of the LB19 data set (whose standard deviation is about a tenth of a beam or ~ 5 mas).

In addition to the correction on the alignment procedure, the scheduling block from Dec. 6, 2017, was missing in the images for the IB17 data set reprocessed in Casassus & Cárcamo (2022), who therefore included only 2/3 of the available data set. The

⁶See Data availability section.

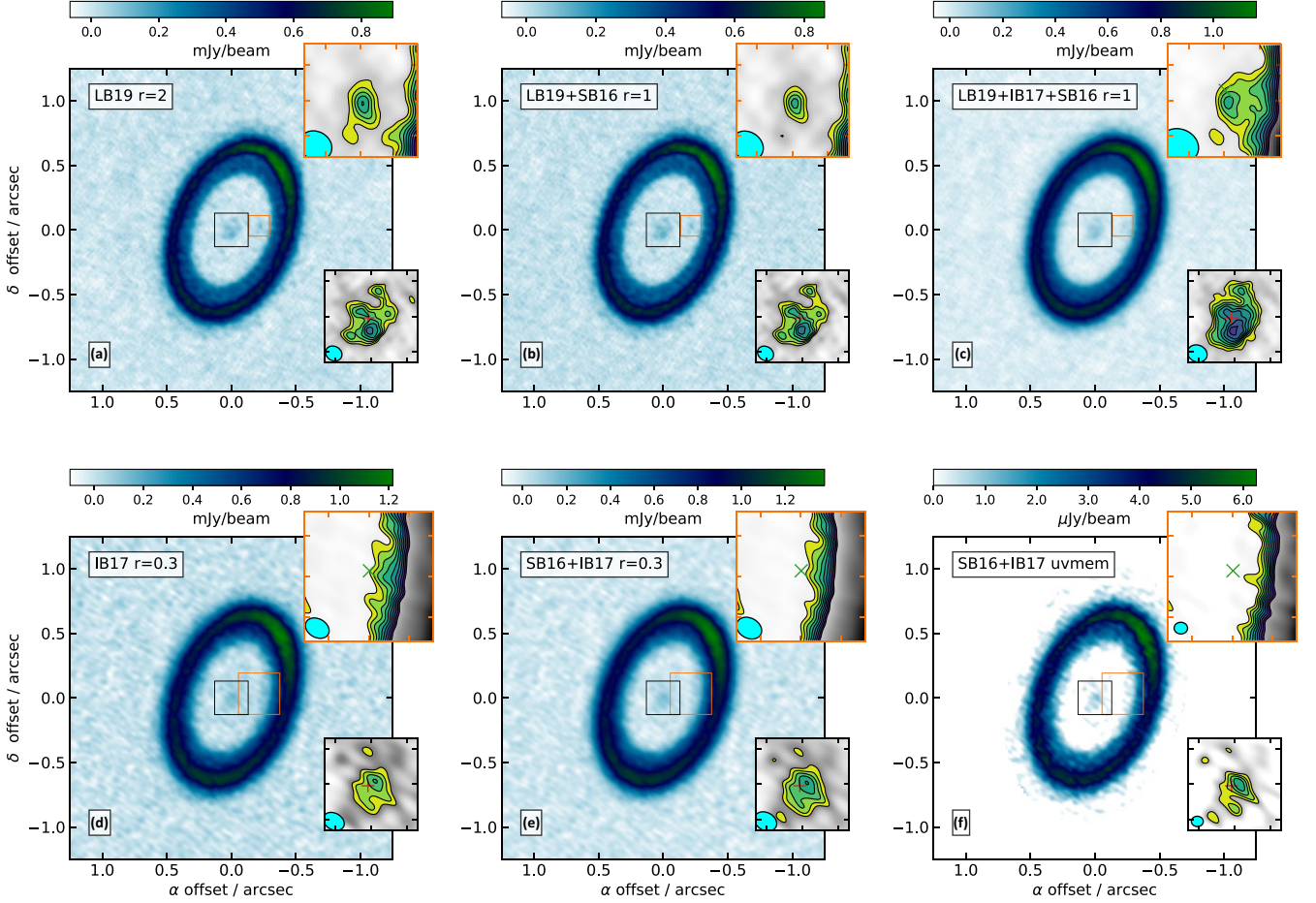


Figure D1. Annotations follow from fig. 4 in Casassus & Cárcamo (2022), except for the red cross in the insets on the inner disc, which is now pointed at the latest *Gaia* coordinates for PDS 70. The updated beam and noise values follow. (a) Clean beam $\Omega_b = 0''.048 \times 0''.040 / 61$ deg. The noise in the residual image is $\sigma = 16.6 \mu\text{Jy beam}^{-1}$. (b) $\Omega_b = 0''.047 \times 0''.039 / 57$ deg, $\sigma = 15.5 \mu\text{Jy beam}^{-1}$. (c) $\Omega_b = 0''.056 \times 0''.047 / 67$ deg, and $\sigma = 13.1 \mu\text{Jy beam}^{-1}$. (d) $\Omega_b = 0''.062 \times 0''.046 / 60$ deg, and $\sigma = 25.9 \mu\text{Jy beam}^{-1}$. (e) $\Omega_b = 0''.066 \times 0''.050 / 61$ deg, and $\sigma = 23.8 \mu\text{Jy beam}^{-1}$. (f) approximate resolution of 1/3 the natural weight beam (Cárcamo et al. 2018), or $\Omega_b \approx 0''.033 \times 0''.029 / 88$ deg. The contours start at 3σ , where $\sigma = 0.16 \mu\text{Jy pix}^{-1}$ is a representative noise level (with 4 mas pixels).

incorporation of this scheduling block improves the sensitivity of the IB17 images, and results in tighter constraints on the absence of PDS 70c in the IB17 data. The corrected images are shown in Fig. D1.

A final correction to the analysis presented in Cárcamo et al. (2018) concerns the choice of reference frequency for multifrequency synthesis. In the UVMEM imaging package (Cárcamo et al. 2018), multifrequency synthesis is implemented with two options. The user can select to fit a spectral index map $\alpha(\vec{x})$ to the data, or use a single and constant spectral index value α to propagate the model visibilities to all frequencies (in specific intensity units, i.e. $I_\nu = I_s(\nu/\nu_s)^\alpha$). We usually adopt a flat spectral index, $\alpha = 0$, but Casassus & Cárcamo (2022) opted to fix $\alpha = 3$, with a reference frequency taken as the median of the centroid frequencies of all spectral windows in the concatenated data sets. This choice of reference frequency is slightly different from the default in CASA `tclean`, which uses the middle frequency. We have now unified the choice of frequency, as required for image restoration. With this correction the point source in LB19 coincident with PDS 70c is now also visible in the concatenation LB19 + IB17 + SB16 (see Fig. D1c).

The noise level in the residuals for the SB16 + IB17 image is $23.9 \mu\text{Jy beam}^{-1}$ (versus $31.9 \mu\text{Jy beam}^{-1}$ in our original pub-

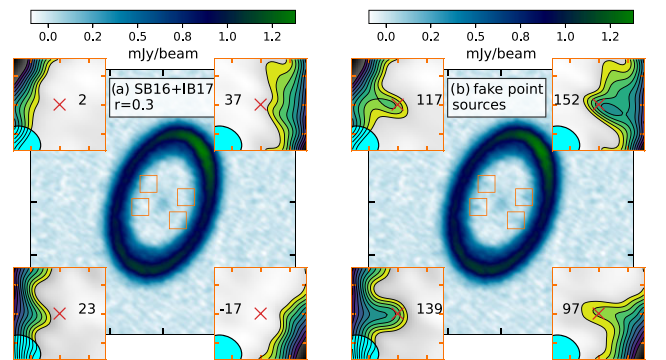


Figure D2. Annotations follow from fig. 6 in Casassus & Cárcamo (2022).

lication). The point source coincident with PDS 70c in the LB19 data set, with peak flux $118.5 \mu\text{Jy beam}^{-1}$ (from Fig. D1a), should have been picked up in IB17 at 5.0σ . The point source injections tests are accordingly updated in Fig. D2. With these new numbers, if we assign a 3σ upper limit flux for PDS 70c in IB17, then it was fainter by 40 per cent \pm 8 per cent relative to LB19 (versus 42 per cent \pm 13 per cent in the original publication).

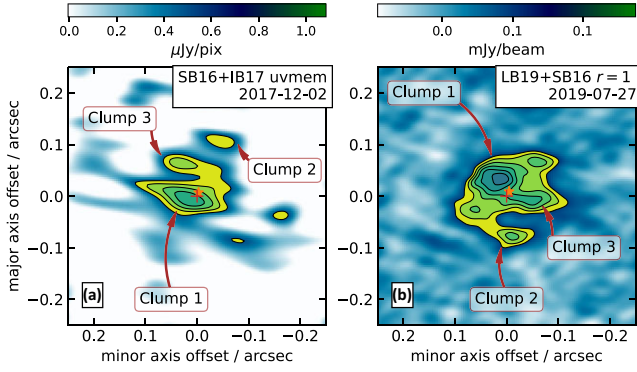


Figure D3. Annotations follow from fig. 7 in Casassus & Cárcamo (2022), except that the red plus sign is now centred on the ring centroid (at the origin of coordinates), while the orange star indicates the position of the star.

An update on the face-on views of the inner disc, and its variability, is given in Fig. D3, including the updated stellar position. The relative pointing accuracy of the multi-epoch data, as estimated from VISALIGN, is ~ 0.4 mas, but the absolute pointing accuracy of the LB19 data set is ~ 5 mas and affects both epochs equally (in the same direction). The accuracy on the position of the ring centroid is 0.5 mas in SB16 + LB19 and 0.7 mas in SB16 + IB17. The offset between the nominal stellar position and the ring centroid is 8 mas in IB17, and 10 mas in LB19.

In summary, the improvements to the analysis of the multi-epoch radio-continuum data from PDS 70 lead to tighter constraints on the variability of PDS 70c. The associated point source is variable by at least 40 ± 8 per cent in 1.75 yr, assigning the upper limit flux of 3σ in the 2017.

This paper has been typeset from a $\text{\TeX}/\text{\LaTeX}$ file prepared by the author.